Supporting Information (SI) Appendix

Direct force measurements reveal protein Tau confers short-range attractions and isoform-dependent steric stabilization to microtubules

Peter J. Chung, Myung Chul Choi, Herbert P. Miller, H. Eric Feinstein, Uri Raviv, Youli Li, Les Wilson, Stuart C. Feinstein, and Cyrus R. Safinya

SI Table S1. Selected constants, values, and variables used for theoretical estimates

Symbol	Value	Description	Units
a	7.8	Effective radius of depleting polymer	nm
c_s	0.075	Equivalent monovalent salt concentration of PEM50	nm^{-3}
d_g^{CTT}	4.5	Grafting distance between C-terminal tails	nm
d_g^{Tau}	$6.4 \times \Phi_{Tau}^{-1/2}$	Grafting distance between Tau as a function of Φ_{Tau}	nm
D_{PRR}	1	Height of proline-rich region of Tau	nm
ε_0	8.854×10^{-12}	Vacuum permittivity	$m^{-3}\ kg^{-1}\ s^4\ A^2$
ε_R	80	Relative permittivity of solution at 298K	
$f_{3RL,PD}$	-0.118	Net ionization fraction, proj. domain of 3RL	
$f_{3RM,\ PD}$	-0.117	Net ionization fraction, proj. domain of 3RM	
$f_{3RS,\ PD}$	-0.082	Net ionization fraction, proj. domain of 3RS	
f_{CTT}	0.5	Average net ionization fraction, C-terminal tail of tubulin	
f_{PRR}	0.138	Net degree of ionization, proline-rich region of Tau	
Φ_{Tau}		Tau to tubulin-dimer molar ratio	
κ	1/.85	Inverse of Debye-Hückel length for PEM50	nm^{-1}
k_B	1.38×10^{-23}	Boltzmann's constant	$m^2\ kg\ s^{-2}\ K^{-1}$
L_{CTT}	3.7	Calculated length of tubulin C-terminal tail	nm
l_B	0.7	Bjerrum length	nm
λ_D	0.85	Debye-Hückel length for PEM50 + 25 mM KCl	nm
$N_{3RL,PD}$	153	Number of residues in proj. domain of 3RL	
$N_{3RM,PD}$	124	Number of residues in proj. domain of 3RM	
$N_{3RS,PD}$	92	Number of residues in proj. domain of 3RS	
N_{CTT}	19.5	Average residues of tubulin C-terminal tail	
ν	0.588	Flory exponent for random coil of amino acids	
$Q_{3RTau\text{-}PD}$	22.5	Net charge of 3R- Tau without the projection domain	e
$Q_{4RTau\text{-}PD}$	26	Net charge of 4R- Tau without the projection domain	e
R_{MT}	12.5	Microtubule outer radius	nm
r_g		Radius of gyration	nm
r_0	0.1927	Characteristic residue length for random coil of amino acids	nm
σ_{MT}	-0.497	Surface charge density of tubulin dimer	$e\ nm^{-2}$
$\sigma_{MT\text{-}CTT}$	-0.387	Surface charge density of tubulin dimer without CTT	$e\ nm^{-2}$
$\sigma_{MT\text{-}CTT,3RTau\text{-}PD}$	$-0.387+ 0.253\times\Phi_{Tau}$	Surface charge density of tubulin dimer without CTT and bound Tau (without PD) (Only for $0\leq\Phi_{Tau}\leq0.1$)	$e\ nm^{-2}$
T	298	Temperature	K

SI Note S1| *Theoretical estimates of inter-microtubule forces*
The basic forces between two microtubules (MT) in our system involve attractive depletion forces (due to 20,000 molecular weight polyethylene-oxide, or 20k PEO) and repulsive forces due the electrostatic and steric forces of MTs and Tau.

S1.1 Depletion Forces on Cylinders by Ideal Polymers
Depletion forces arise when large colloidal particles (in our case, microtubules [MTs]) are suspended in a dilute solution of osmotic depletants (20k PEO). The depletants are preferentially excluded from the vicinity of the colloidal particles due to its inability to get closer than its effective radius, *a* (Figure S1.1). In the low-concentration limit (dilute regime), the monomers apply an ideal gas-like osmotic pressure $\prod_{osm}=ck_BT$ (where c is the number density of 20k PEO) owing to a reduction of excluded volume when excluded volumes overlap (1).

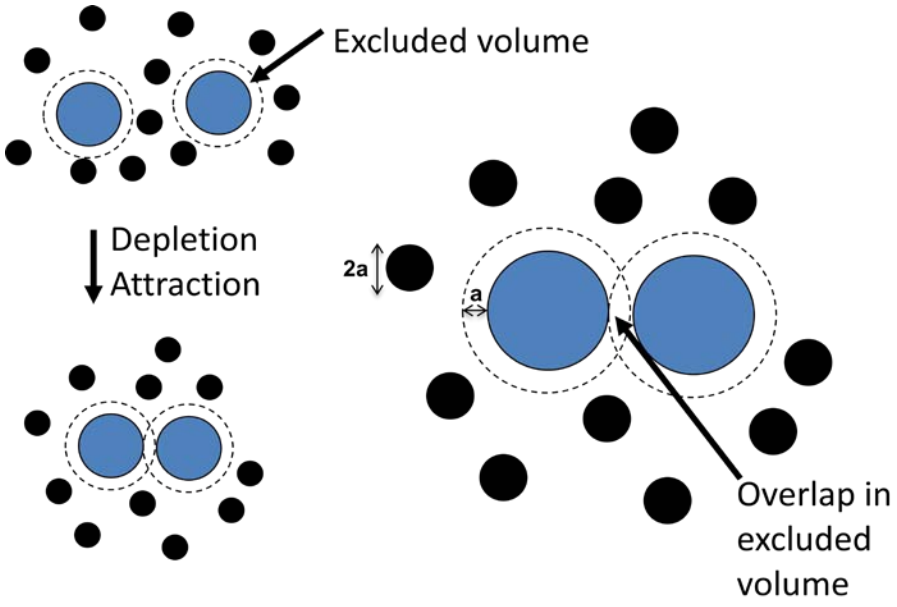

Figure S1.1| An axial view of parallel cylinders bundled by depletion attraction. The 20k PEO (black circles) is barred from the excluded volume (dashed line) around the microtubules (blue circles). The overlap of these two excluded volumes results in an excess volume available for the 20k PEO, leading to an entropically induced attraction between microtubules (equivalently, the removal of 20k PEO depletants results in an excess PEO density around the MTs, pushing them together).

The depletion energy per unit length (at the dilute limit) takes the form (2):

$$V_{depletion} = -ck_BTA(H, R, a) \qquad \text{(Equation S1.1)}$$

where *A(H)* is the overlap of the excluded area (cross section of overlap of the excluded volume) as a function of the distance *H* between the surface of two circular cylinders of radius *R* (for MTs, R=12.5nm), surrounded by monomers of radius *a* (for 20k PEO, the effective depletant radius for a polymer of radius of gyration, r_g = 6.9 nm, $a = \frac{2r_g}{\sqrt{\pi}}$ = 7.8 nm) (3, 4). By constructing two circles of radius *R′* and center-to-center distance *d* (Figure S1.2), the known formula (1) for circular segments is used to calculate the excluded area with the appropriate translation, $R' \rightarrow R + a$ and $d \rightarrow H + 2R$

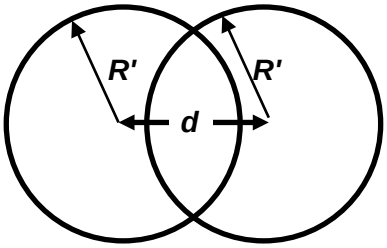

Figure S1.2| The overlap of two circles as a function of center-to-center distance. The lens shaped region is a sum of two circular segments.

$$A(d,R') = 2R'^2\cos^{-1}\left(\frac{d}{2R'}\right) - \frac{d}{2}\sqrt{4R'^2 - d^2}$$

$$A(H,R,a) = 2(a+R)^2\cos^{-1}\left(\frac{H+2R}{2(a+R)}\right) - \frac{(H+2R)}{2}\sqrt{(2a-H)(2a+H+4R)}$$

$$A(H,R,a) = (a+R)^2\left(2\cos^{-1}\left(\frac{H+2R}{2(a+R)}\right) - \frac{(d+2R)\sqrt{(2a-H)(2a+H+4R)}}{2(a+R)^2}\right) \qquad \text{(Equation S1.2)}$$

$$A(H,R,a) = \begin{cases} (a+R)^2\left(2\cos^{-1}\left(\frac{H+2R}{2(a+R)}\right) - 2\left(\frac{H+2R}{2(a+R)}\right)\sqrt{1-\left(\frac{H+2R}{2(a+R)}\right)^2}\right) & 0 < H \le 2a \\ 0 & H > 2a \end{cases}$$

Which is mathematically equivalent to results of previous work (5)

$$A(H,R,a) = \begin{cases} (a+R)^2(\Theta - \sin(\Theta)) & 0 < H \le 2a \\ 0 & H > 2a \end{cases} \qquad \text{(Equation S1.3)}$$

Where $\Theta = 2\sin^{-1}\left(\frac{\sqrt{(2a-H)(2a+H+4R)}}{2(a+R)}\right)$. This is shown by setting $x = \left(\frac{H+2R}{2(a+R)}\right)$ and using the identities $2x\sqrt{1-x^2} = \sin\left(2\sin^{-1}\left(\sqrt{1-x^2}\right)\right)$ and $Cos^{-1}(x) = Sin^{-1}\left(\sqrt{1-x^2}\right)$ such that Equation S1.2 becomes

$$A(H,R,a) = (a+R)^2\left(2\sin^{-1}\left(\sqrt{1-x^2}\right) - \sin\left(2\sin^{-1}\left(\sqrt{1-x^2}\right)\right)\right) \qquad \text{(Equation S1.4)}$$

By setting $\Theta = 2\sin^{-1}\left(\sqrt{1-x^2}\right) = 2\sin^{-1}\left(\frac{\sqrt{(2a-H)(2a+H+4R)}}{2(a+R)}\right)$, we get exact published results as before. Thus, the potential energy normalized (in the dilute regime) is:

$$V_{depletion}(H) = -ck_BTA(H,R,a) \qquad \text{(Equation S1.5)}$$

However, it is important to note that this is a simplified derivation; in treating PEO as an ideal gas (dilute regime), interactions between individual polymers (2nd and higher order virial-coefficients) are not taken into account. Experimental measurements are needed to obtain the osmotic pressure (Π) of polymer-induced depletion forces. Thus, the depletion-attraction potential energy used in our modeling was:

$$V_{depletion}(H) = -\Pi A(H, R, a) \qquad \text{(Equation S1.6)}$$

Π is the measured depletant osmotic pressure ($\lim_{c\to 0} \Pi = ck_BT$). Fortunately, measurements of the osmotic pressure for the dilute and semi-dilute regime of 20k PEO have been reported (6) (Figure S1.3 and caption), allowing quick translation between wt% of 20k PEO and osmotic pressure values.

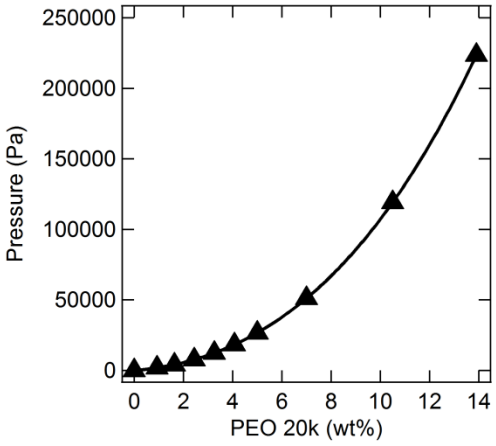

Figure S1.3| The osmotic pressure measured for increasing wt% of 20k PEO. Experimentally derived data points (triangle markers) for the osmotic pressure (Pa) is used to obtain a best-fit line to extrapolate pressures for any given wt% of 20k PEO, where $Log_{10}(\Pi) = .57 + 2.75 \times (PEOwt\%)^{.21}$

S1.2 Electrostatic potential energy between two charged cylinders (hard cylinder model)

To first order, the electrostatic repulsive forces between MTs can be modeled as the potential energy between two parallel, charged cylinders. This is calculated by applying the Derjaguin approximation (7) (which has its limits, but is used for simplicity) to relate the potential energy between planar surfaces to curved surfaces of radius R:

$$V_{cyl}(H) = \sqrt{R}\int_{H}^{\infty} V_{plane}(h)\frac{dh}{\sqrt{h-H}} \qquad \text{(Equation S1.7)}$$

Where $V_{plane}(h)$ (energy per unit area) and $V_{cyl}(H)$ (energy per unit length) are the potential energies for surface-to-surface distances for parallel planes and cylinders, respectively (Figure S1.4).

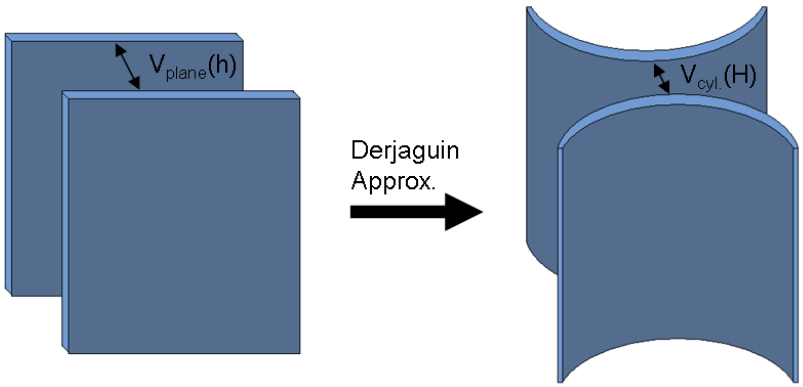

Figure S1.4| The Derjaguin approximation takes planar potential energies and converts them to equivalent potential energies for curved surfaces. In our particular case, the electrostatic planar potential for surface-to-surface distance *h* is "bent" to an equivalent potential for two parallel cylindrical surfaces with surface-to-surface distance *H*

The potential energy per unit area between two charged surfaces (in the Debye-Hückel regime) with "hard" surface charge density σ in an electrolyte solution (of permittivity $\varepsilon_r\varepsilon_0$) is (1)

$$V_{plane}^{hard}(h) = \frac{2\sigma^2 e^{-\kappa h}}{\kappa \varepsilon_r \varepsilon_0} \qquad \text{(Equation S1.8)}$$

Where κ is the inverse of the Debye-Hückel length, the characteristic decay length of electrostatic potential energy in an electrolyte solution of concentration c_s. For monovalent salt concentration c_s, the Debye-Hückel length is calculated (1) as $\lambda_D = 1/\kappa = \left[\varepsilon_r \varepsilon_0 k_B T/(2e^2 c_s)\right]^{1/2}$. Inserting Equation S1.8 into Equation S1.7 yields the cylindrical potential energy per unit length for surface-to-surface distance H, as calculated by Ohshima and Hyono (8):

$$V_{cyl}^{hard}(H) = \frac{2\sqrt{\pi R}\sigma^2}{\varepsilon_r \varepsilon_0 \kappa^{3/2}} Li_{1/2}(e^{-\kappa H}) \qquad \text{(Equation S1.9)}$$

Where $Li_{1/2}(z) = \sum_{k=1}^{\infty} z^k / k^{1/2}$, the polylogarithm function of order 1/2. The reduced potential energy per unit length rewritten for our system in terms of cylinder radius (microtubule radius, R_{MT}≈12.5nm), Debye-Hückel length λ_D =.85nm for PEM50 (50 mM PIPES, 1mM $MgCl_2$ and 1 mM EGTA at pH 6.8 with 75 mM NaOH) with 25 mM KCl added (equivalent to a 100 mM solution of 1:1 electrolyte plus 1 mM of $MgCl_2$), surface charge density σ_{MT}, and salt concentration c_s≈.075nm^{-3} (for a monovalent salt equivalent to PEM50 at pH 6.8 with 25 mM added KCl):

$$\frac{V_{cyl}^{hardMT}(H)}{k_B T} = \frac{\sqrt{\pi R_{MT}}\,\sigma_{MT}^2 \kappa^{1/2}}{e^2 c_s} Li_{1/2}(e^{-\kappa H}) \qquad \text{(Equation S1.10)}$$

The surface charge density σ, absent a physical measurement, is usually calculated from the net charge of the sequence without accounting for partial neutralization by counterions. Measurements of microtubule electrophoretic movement in microchannels provide an estimate of the partial counterion neutralization (9). At pH 6.9, the bare-charge of the tubulin (Q_{bare}) and bound nucleotides/ions was calculated to be -

50e per dimer, but the effective charge (Q_{eff}) was measured as -23e per dimer. Thus, we calculate the effective charge renormalization prefactor $r = Q_{eff}/Q_{bare} = 0.46$.

In our experiments the bare charge of α-tubulin (NCBI protein database: NP_001159977.1) and β-tubulin (NP_001040014.1) with bound nucleotides/ions was calculated to be -21.7e and -22.6e, respectively, at pH 6.8 (via http://protcalc.sourceforge.net/), giving a sum bare-charge of -44.3e per tubulin-dimer. As both experiments were in similar buffer conditions, we use the effective charge renormalization prefactor r to calculate the effective charge $Q_{eff} = r\,Q_{bare} \approx$ -20.4e per tubulin-dimer. As the dimer area ≈ 41 nm^2 (product of dimer height, 8 nm, and protofilament-protofilament distance, 5.13 nm) (10), this gives an effective renormalized suface charge density σ_{MT}= -0.497e nm^{-2}.

S1.3 MT bundling using the hard cylinder model

Equation S1.6 and S1.10 are used to model the pairwise interaction of microtubules using depletion attraction and the hard cylinder model for microtubules.

$$V_{MT}(H) = V_{depletion}(H) + V_{cyl}^{hardMT}(H) \qquad \text{(Equation S1.11)}$$

The sum of the potential energies (Equation S1.11) is plotted as a function of wt% of 20k PEO (Figure S1.5). If we consider the average length of microtubules (~2 µm, Figure S1.6) and expect the bundled state to correspond to a potential energy depth of 5 to 10 k_BT, the model predicts bundling at a wt% of 20k PEO as low as 0.15. As the nematic (non-bundled) phase is experimentally observed at a higher wt% of 20k PEO (0.25), the model does not capture the magnitude of repulsive forces.

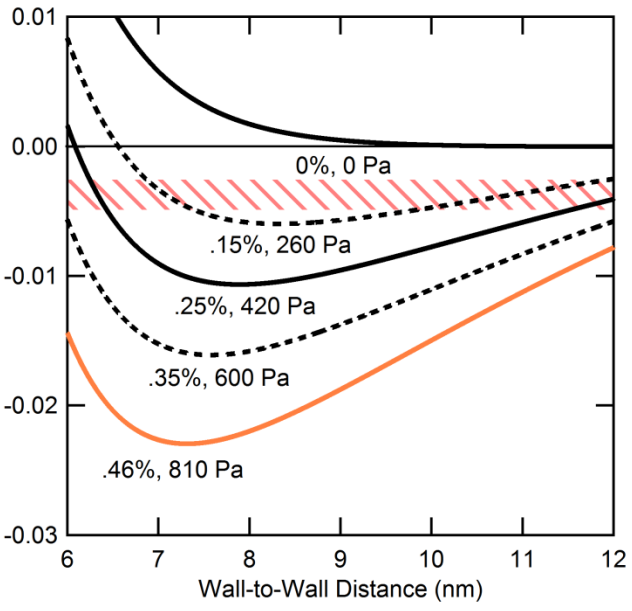

Figure S1.5| The energy per unit length curves against the wall-to-wall distance using the simple charged-cylinder model for MTs. Curves derived from the model (equation S1.10) are plotted for actual PEO wt% used in experiments (solid lines) and in-between concentrations (dashed lines). Colors (from black to orange) are coordinated with data in fig. 3 (Φ_{Tau}=0). If the bundled state corresponds to a potential energy depth of 5 to 10 k_BT (the pink-striped zone) for 2 µm length MTs (see Fig. S1.6), the model predicts bundling would occur at .15 wt% of 20k PEO (and above) while experimentally bundling is seen between 0.25 and 0.46 wt% of 20k PEO (orange curve).

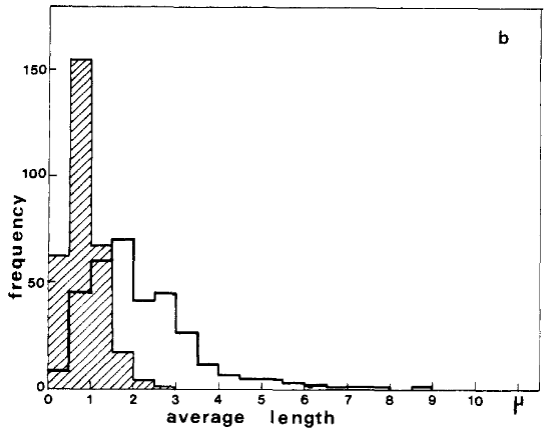

Figure S1.6| The length distributions for taxol-stabilized microtubules. Near stoichiometric amounts of taxol to tubulin, the average length of microtubules is identified using electron microscopy and plotted after 1 min (hatched bars) and 30 mins (thick bars) (11). The average length is taken to be 2 μm

S1.4 Electrostatic potential energies between two soft, charged cylinders

It is apparent that the modeling of microtubules as charged "hard" cylinders underestimates the repulsive component, thus requiring a more advanced model. From our knowledge of tubulin crystallography (10), MTs do not have a constant charge density. Most of the charge is located on the C-terminal tails (CTT) of both α- and β- tubulin (18 and 21 residues, respectively (12), both with an average ionization fraction $f_{CTT}\approx 0.5$). As a result of this high-charge density, not only does it make MTs akin to a polyelectrolyte-grafted colloids (Figure S1.7) but the charge must be renormalized (with prefactor r), as in S1.3 with the MT surface. Due to the intrinsically disordered nature of the CTT, the height of the CTT is not well defined but is estimated to be $L_{CTT}\approx 4$ nm from simulation data (13), with an expanded conformation expected by theory (14).

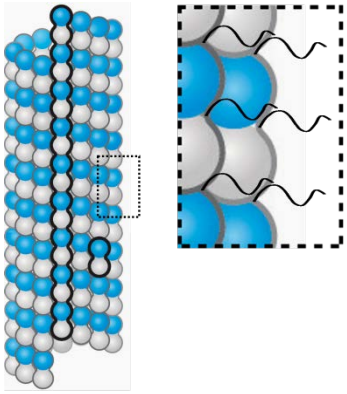

Figure S1.7| A close-up view of the microtubule surface reveals positively-charged C-terminal tails of α- and β-tubulin. While microtubules can be approximated to be hollow cylinders made up of tubulin with constant charge density, a more appropriate model takes into account the charge found in the CTTs that project off the microtubule surface.

A more sophisticated model for microtubules accounts for the polyelectrolyte layer above the microtubule surface, necessitating a shift from the hard cylinder model (with surface charge density,σ) to a soft cylinder (with volume charge density,ρ) model. The potential energy per unit area for a soft planar charged surface is (8)

$$V_{plane}^{soft\ CTT}(h)=\frac{\rho^2\sinh^2(\kappa L)}{2\kappa^3\varepsilon_r\varepsilon_0}\left[\coth\left(\frac{\kappa h}{2}\right)-1\right] \qquad \text{(Equation S1.12)}$$

Where L is the height of the polyelectrolyte layer and h is the surface-to-surface distance, *not* including the polyelectrolyte layer. Utilizing the Derajaguin approximation (equation S1.7), the soft cylinder model is calculated by Ohshima (8):

$$V_{cyl}^{soft\ CTT}(H) = \frac{2\sqrt{\pi R}\rho^2}{\varepsilon_r \varepsilon_0 \kappa^{7/2}} \sinh^2(\kappa L) Li_{1/2}(e^{-\kappa H}) \qquad H \geq 2L \qquad \text{(Equation S1.13)}$$

Where the volume charge density is the product of ionization fraction (f_{CTT}≈1/2), average number of residues in the CTT (N_{CTT}=19.5), and renormalization prefactor r, divided by the volume occupied by the CTT (simplified as the product of square of the CTT grafting distance [$(d_g^{CTT})^2$ ≈21 nm^2] and the height of the CTT [L_{CTT}=4 nm]):

$$\rho = \frac{erfN}{d_g^2 L} \qquad \text{(Equation S1.14)}$$

Equation S1.13 can be rewritten using the appropriate variables. To include the limit where $H < 2L$, the polyelectrolyte layer height is compressed to half the surface-to-surface distance, by geometry.

$$\frac{V_{cyl}^{softCTT}(H)}{k_B T} = \begin{cases} \dfrac{\sqrt{\pi R_{MT}}\left(\dfrac{erf_{CTT} N_{CTT}}{\left(d_g^{CTT}\right)^2 L_{CTT}}\right)^2}{c_s \kappa^{3/2}} \sinh^2(\kappa L_{CTT}) Li_{1/2}(e^{-\kappa H}) & H \geq 2L_{CTT} \\ \dfrac{\sqrt{\pi R_{MT}}\left(\dfrac{erf_{CTT} N_{CTT}}{\left(d_g^{CTT}\right)^2 H}\right)^2}{c_s \kappa^{3/2}} \sinh^2\left(\dfrac{\kappa H}{2}\right) Li_{1/2}(e^{-\kappa H}) & H < 2L_{CTT} \end{cases} \qquad \text{(Equation S1.15)}$$

S1.5 MT bundling using the soft cylinder model

In our more advanced model (utilizing equation S1.15), contributing factors include the depletion attraction (from the 20k PEO, equation S1.5), "hard" electrostatic repulsion (from the remaining charge on the MT surface [where $\sigma_{Tub\text{-}CTT}$=-0.387e nm^{-2}], equation S1.9), and soft electrostatic repulsion from the tubulin CTT (equation S1.14)

$$V_{MT}^{Total}(H) = V_{Depletion}(H) + V_{cyl}^{hardMT}(H) + V_{cyl}^{soft\ CTT}(H) \qquad \text{(Equation S1.16)}$$

The system potential energies were also plotted over a range of low wt% of 20k PEO (Figure S1.8). The model captures the correct wt% of 20k PEO, which can be seen in a component breakdown of each potential energy contribution (Figure S1.9).

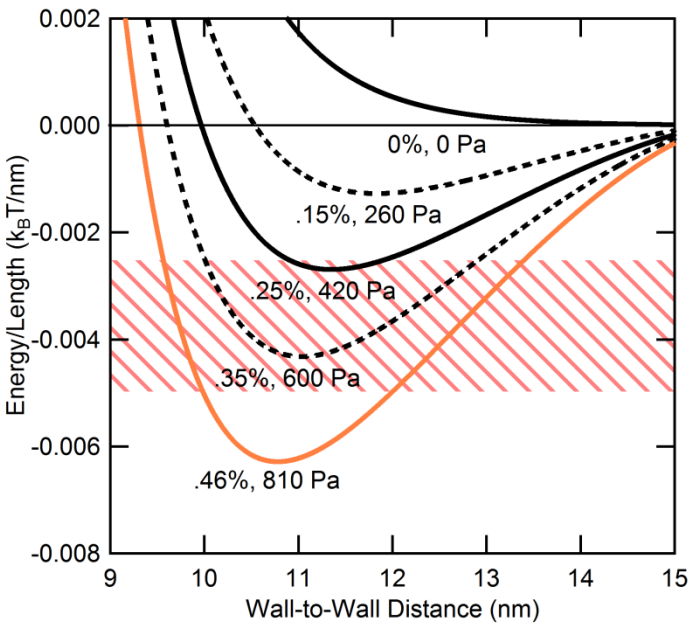

Figure S1.8| The energy per unit length curves against the wall-to-wall distance utilizing the soft-cylinder model. Curves derived from the model (equation S1.15) are plotted for actual PEO wt% used in experiments (solid lines) and in-between concentrations (dashed lines). Colors (from black to orange) are coordinated with data in fig. 3 (Φ_{Tau}=0). If the bundled state corresponds to a potential energy depth of 5 to 10 k_BT (the pink-striped zone) for 2 μm length MTs (see Fig. S1.6), the model predicts bundling would occur at .46 and .35 wt% of 20k PEO, which is experimentally recapitulated (orange curve).

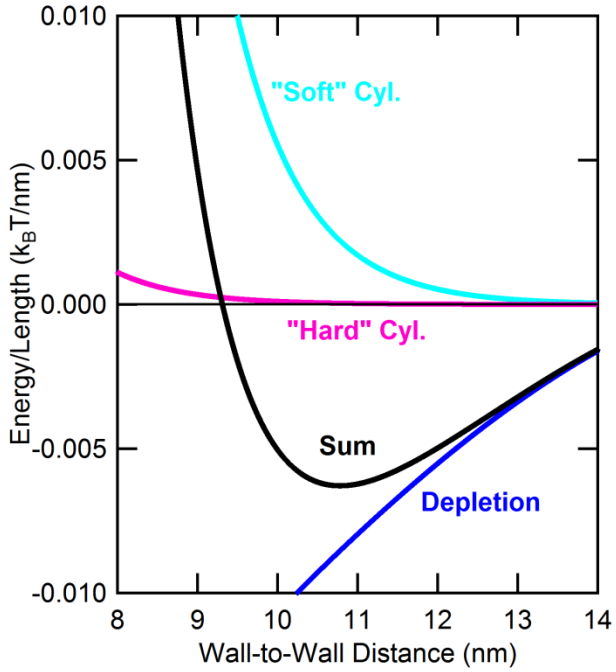

Figure S1.9| Component breakdown of the potential energy per unit length for 0.46 wt% of 20k PEO. Note the dominant contribution of the soft-cylinder, owing to the short Debye-Hückel length which more effectively screens the hard-cylinder interactions.

SI Note S2| *Treatment of Tau on Microtubules*

S2.1 Height of Tau protruding normal to the microtubule surface

While treatment of the C-terminal tails of tubulin is relatively straightforward, models of Tau are more involved because of its polyampholytic nature. While it is known the microtubule-binding repeats are closely bound to the surface, less is known about the N- and C- terminal tails of Tau (NTT and CTT, respectively). Due to the relative size of the Tau NTT (196 residues for the shortest isoform) compared to the Tau CTT (73 residues) and the prior knowledge that the projection domain of the NTT is known to project off the MT surface (15), only the contributions of the Tau NTT is considered.

The NTT consists of a highly-charged polyampholytic projection domain (PD, ~40% of residues charged) and a weakly-cationic proline-rich region (PRR, ~20% of residues charged). Simulations (16, 17) suggest that the PRR is weakly-bound to the highly-anionic MT surface and the PD assumes an extended conformation normal to the MT surface. The dramatic increase in pressure required to bundle microtubules for the –M and –L Tau isoforms (see Fig. 3, main paper) suggest that Tau underwent a conformational change on the MT surface at Φ=1/13 for the –L isoforms and Φ=1/10 for the –M isoforms. This occurs when the diameter of Tau protein on the MT surface approaches the distance between Tau proteins on MTs.

Even though Tau is physisorbed on the MT surface, binding data (18) indicates that the concentration at which Tau is mixed with tubulin is the same concentration upon which Tau is bound to the MT surface (Up until Φ=1/5 to 1/3). Thus, we treat Tau as essentially grafted to the MT surface, where

$$d_g^{Tau} = \frac{4.5}{2\sqrt{\frac{\Phi_{Tau}}{2}}}\,[\text{nm}] \qquad \text{(Equation S2.1)}$$

4.5 nm is the average tubulin monomer-monomer distance and the factor of 2 arises because Φ is a dimer ratio. The lowest Φ at which the transition is observed corresponds to a grafting distance of 20.3 nm and 23.1 nm for –M and –L isoforms of Tau, respectively, which will be used as L_{PD}, or the height of the projection domain. .

The grafting distance (as a proxy for the polyelectrolyte brush height) is clearly an underestimate, as it is more appropriate for the height of Tau prior to the brush transition. However, it will serve as a useful estimate for our models.

S2.2 Treatment of Tau Isoforms with Longer Projection Domains (3RM, 3RL) on microtubules (soft cylinder model)

The 3RM isoform of Tau is also examined using the same system potential energy as before (Equation S1.16) with r = 1 (i.e. where charge renormalization is expected to be negligible because the combination of a low net ionization of the PD together with low Tau coverage leads to a low charge density polyelectrolyte layer surrounding the microtubule) and additional soft potential term for Tau with appropriate variable substitution ($L_{3RM,PD}$=20.3nm, $N_{3RM,PD}$=121, $f_{3RM,PD}$=.120, and equation S2.1) (Figure S2.1).

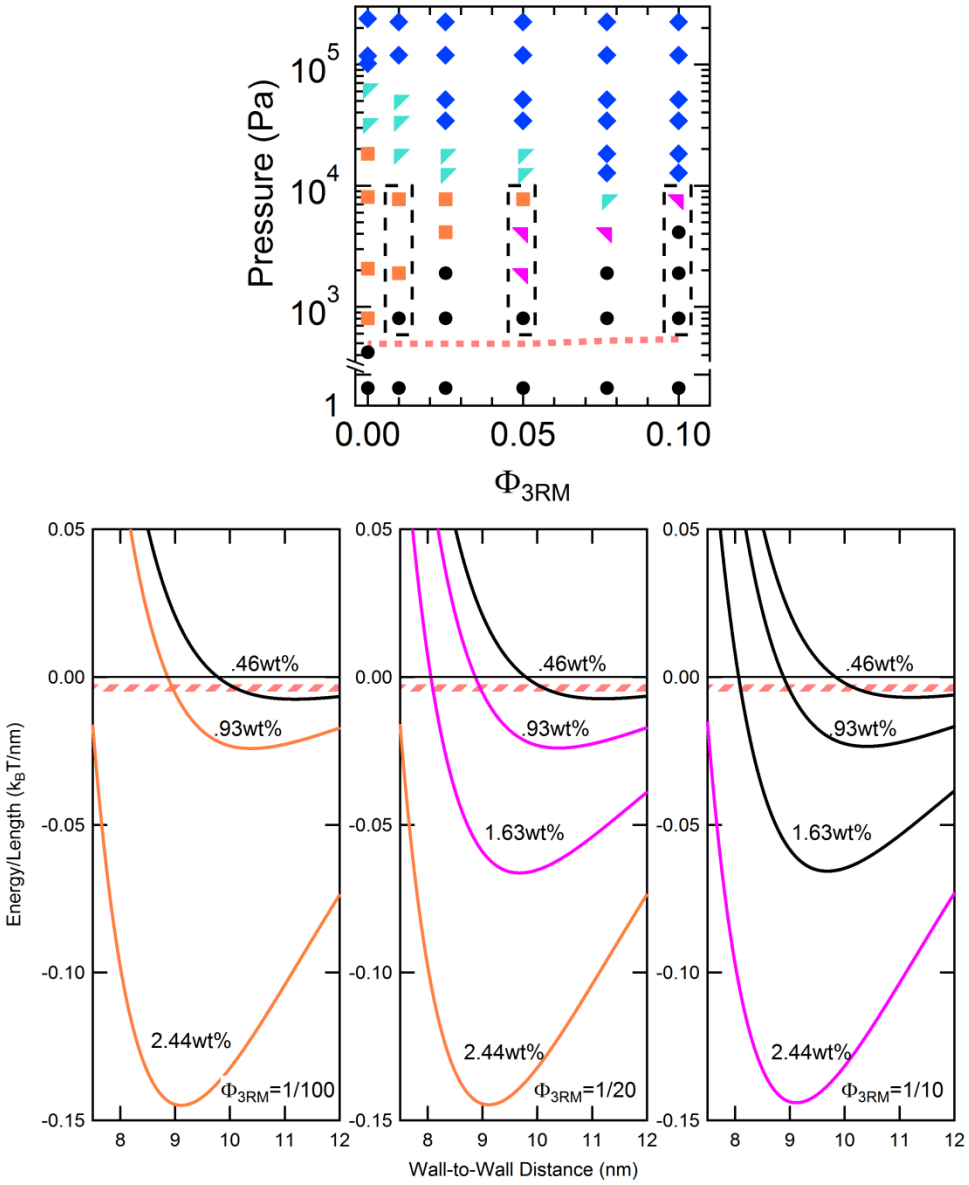

Figure S2.1| The soft cylinder model did not capture the resultant increase in repulsion between microtubules coated with 3RM Tau. At osmotic pressures taken from selected experimental data points (top, dashed box), the normalized potential energy per unit length curves were plotted for Φ_{3RM}=1/100, 1/20, 1/10 (bottom), with the color of each model curve corresponding to phase observed experimentally. The phase diagram (top) has been marked (pink-dashed line) at the pressure where bundling is expected, if bundling is assumed to occur at a potential energy depth of 7.5 k_BT for 2 μm length MTs (see Fig. S1.6). The potential energy curves (bottom) also have a pink-striped zone, which corresponds to a potential energy depth of 5 to 10 k_BT.

The soft cylinder model for the 3RM isoform of Tau does not capture the increase in repulsion, especially at Φ_{3RM}=1/10, where phases that were experimentally observed to be in non-bundled phases

were, by our model, expected to be bundled. The model is similarly applied to the 3RL isoform of Tau, with appropriate substitution of variables ($N_{3RL,PD}$=150, $f_{3RL,PD}$=.120, $L_{3RL,PD}$=23.1 nm) (Figure S2.2).

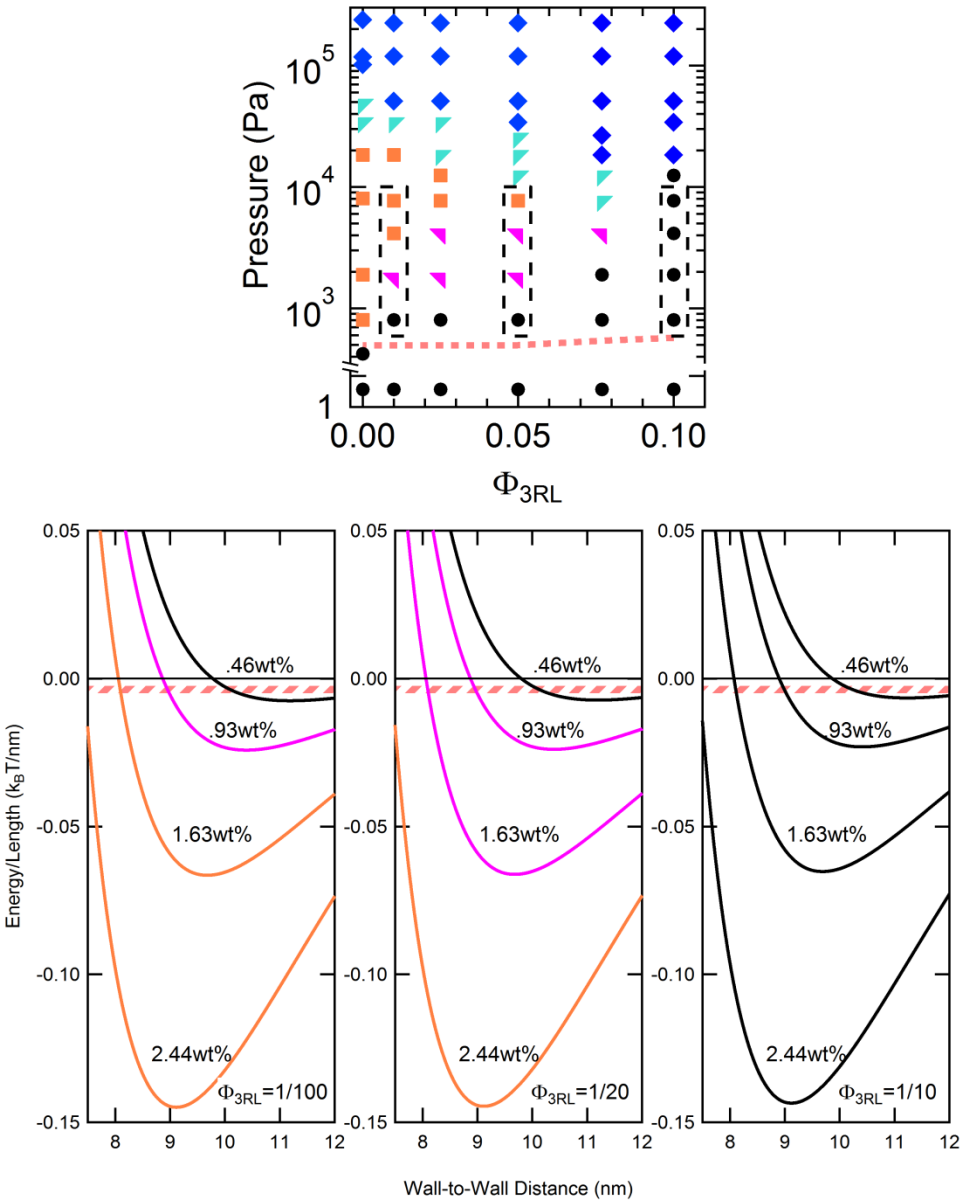

Figure S2.2| The soft cylinder model did not capture the resultant increase in repulsion between microtubules coated with 3RL Tau. At osmotic pressures taken from selected experimental data points (dashed boxes, top), the normalized potential energy per unit length curves were plotted for Φ_{3RL}=1/100, 1/20, 1/10 (bottom), with the color of each model curve corresponding to phase observed experimentally. The phase diagram (top) has been marked (pink-dashed line) at the pressure where bundling is expected, if bundling is assumed to occur at a potential energy depth of 7.5 k_BT for 2 μm length MTs (see Fig. S1.6). The potential energy curves (bottom) also have a pink-striped zone, which corresponds to a potential energy depth of 5 to 10 k_BT.

Upon accounting for the Tau isoforms with the longer projection domains, there was not an appreciable increase in repulsion in the modeled MT-MT interactions. The soft cylinder model broke down for Tau and another model was required to recapitulate the increase in bundling pressure required to bundle MTs with higher coverage of the Tau isoforms with longer projection domains.

S2.3 Treatment of Tau Isoforms with Longer Projection Domains (3RM, 3RL) on microtubules (charged brush model)

The soft cylinder model for Tau is insufficient. Instead, we treat the PD as a brush (with appropriate modifications). While the theory was developed for polyelectrolytes (and not polyampholytes), a polyelectrolyte brush model is used to examine the scaling of the disjoining pressure.

At high grafting density, interactions between polyelectrolytes on the same surface dominate and cause polyelectrolytes to stretch into a brush-like conformation (surface charge effects polyelectrolyte conformation, but the following model is chosen for its simplicity). Previously, Witten and Pincus (19) theorized that for a given polyelectrolyte solution (of counterion concentration c_0), the osmotic pressure in the presence of salt (c_s) is given by

$$P \cong c_0 k_B T \left(\frac{\kappa_0^2}{\kappa_0^2 + \kappa_s^2} \right) \qquad \text{(Equation S2.2)}$$

Where $\kappa_0^2 = 4\pi l_B c_0$ and $\kappa_s^2 = 4\pi l_B (2c_s)$ is the inverse square of the Debye-length of counterions and added monovalent salt, respectively. In the limit of high salt ($\kappa_s^2 >> \kappa_0^2$) the pressure can be solved (20) as a function of as a concentration of monomers ($c_m = N_m (Ld^2)^{-1}$), where N_m is the degree of polymerization and Ld^2 is the space in which the polymers occupy) and net ionization fraction f

$$P \cong c_0 k_B T \left(\frac{\kappa_0^2}{\kappa_s^2} \right) = \frac{k_B T c_0^2}{2c_s} = \frac{k_B T (f c_m)^2}{2c_s} \qquad \text{(Equation S2.3)}$$

The disjoining pressure, Π_{Plane}, as a function of the surface-to-surface distance h is then

$$\Pi_{plane}^{brush} = \frac{k_B T}{2c_s} \left(\frac{2fN}{d_g{}^2 h} \right)^2 \qquad h \le 2L \qquad \text{(Equation S2.4)}$$

The Derjaguin approximation is used as before (but instead, for force) to arrive at the equivalent disjoining pressure for two cylinders[18]

$$\Pi_{cyl}^{brush}(H) = \sqrt{R} \int_H^\infty \Pi_{Plane}^{Brush}(h) \frac{dh}{\sqrt{h - H}} = -\frac{\pi \sqrt{R} k_B T f^2 N^2}{c_s d_g{}^4} \left(\frac{1}{H^{3/2}} \right) \qquad \text{(Equation S2.5)}$$

Equation S2.5 can be integrated to obtain the disjoining potential energy for the appropriate limits

$$V_{cyl}^{brush}(H) = -\int_{H}^{2L} \Pi_{cyl}^{Brush}(H')dH' = \frac{2\pi\sqrt{R}k_B T f^2 N^2}{c_s d_g{}^4}\left(\frac{1}{\sqrt{H}} - \frac{1}{\sqrt{2L}}\right) \qquad \text{(Equation S2.6)}$$

This gives the reduced potential energy, with appropriate insertion of variables (and equation S2.1):

$$\frac{V_{cyl}^{brush,tauPD}(H)}{k_B T} = \begin{cases} \dfrac{2\pi\sqrt{R_{MT}}\, f_{TauPD}^2 N_{TauPD}^2}{c_s\left(d_g^{Tau}\right)^4}\left(\dfrac{1}{\sqrt{H}} - \dfrac{1}{\sqrt{2L_{TauPD}}}\right) & H < 2L_{TauPD} \\ 0 & H \geq 2L_{TauPD} \end{cases} \qquad \text{(Equation S2.7)}$$

The system potential energy is modeled, as before, but the contribution from Tau utilizing the soft cylinder model (4th term) is replaced with a contribution from Tau utilizing the polyelectrolyte brush model (Equation S2.7) and the 2nd term is taken to include remaining anionic surface charge of the MT surface (without the tubulin CTT) and the positive contribution from the bound Tau (which excludes the PD, $\sigma_{MT\text{-}CTT,3RTau\text{-}NT}$=-(-0.387+0.253×$\Phi_{Tau}$) e nm^{-2})

$$V_{MT+Tau}^{Brush} = V_{Depletion} + V_{cyl}^{hardMT,tau} + V_{cyl}^{soft,CTT} + V_{cyl}^{brush,tauPD} \qquad \text{(Equation S2.8)}$$

Applying the charged brush model to the isoforms with the longer projection domains of Tau did recapitulate a jump in 20k PEO required to bundle the microtubules, especially at higher Tau coverages (Figure S2.3 and S2.4). The brush model seemed to be a more appropriate (despite assumptions made!) for high coverages of the Tau isoforms with longer projection domains (3RM, 4RM, 3RL, 4RL).

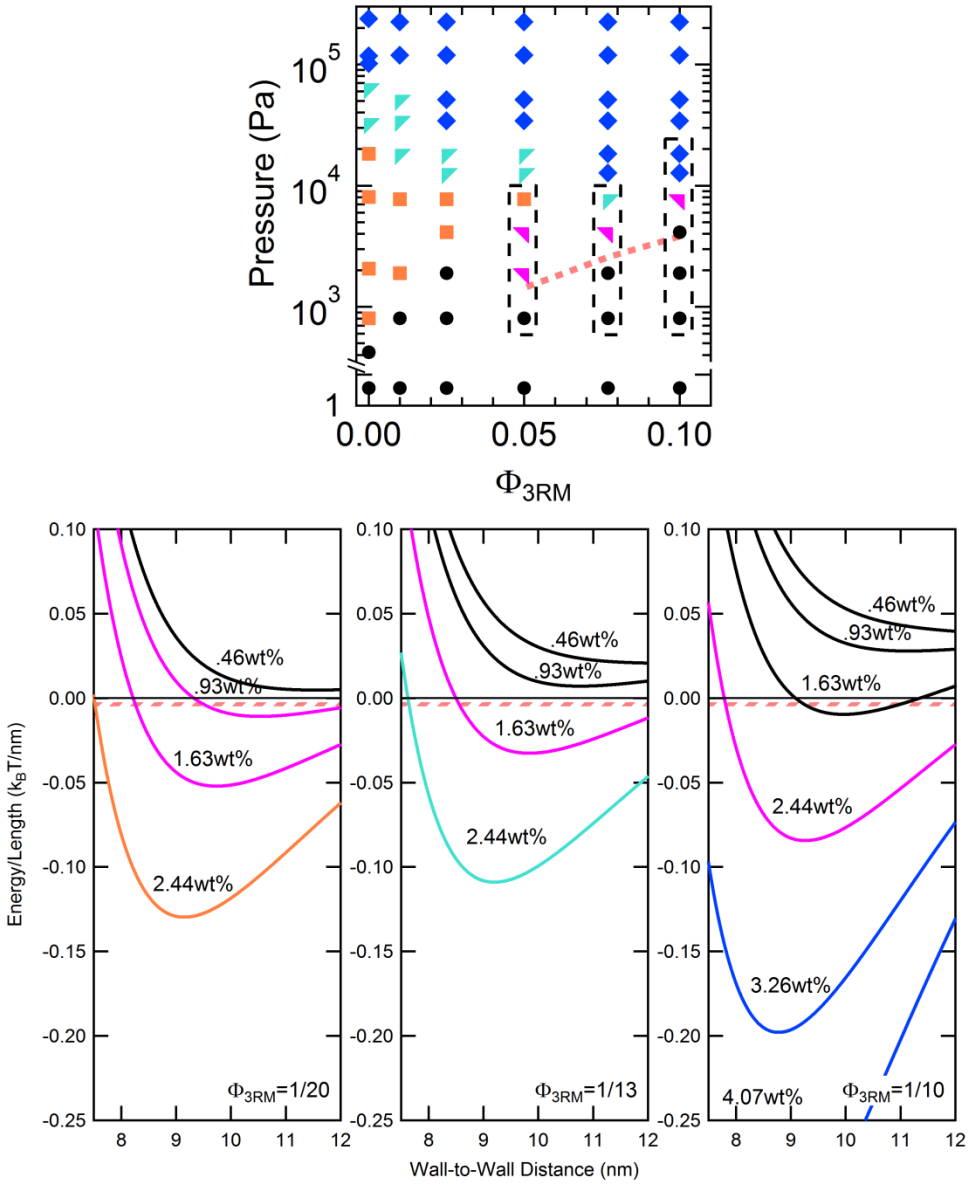

Figure S2.3| The charged brush model for 3RM Tau at higher coverages of Tau is in closer agreement with experimental behavior. At osmotic pressures taken from selected experimental data points (top), the normalized potential energy per unit length curves were plotted for Φ_{3RM}=1/20, 1/13, 1/10 (bottom), with the color of each model curve corresponding to phase observed experimentally. The phase diagram (top) has been marked (pink-dashed line) at the pressure where bundling is expected, if bundling is assumed to occur at a potential energy depth of 7.5 k_BT for 2 µm length MTs (see Fig. S1.6). The potential energy curves (bottom) also have a pink-striped zone, which corresponds to a potential energy depth of 5 to 10 k_BT.

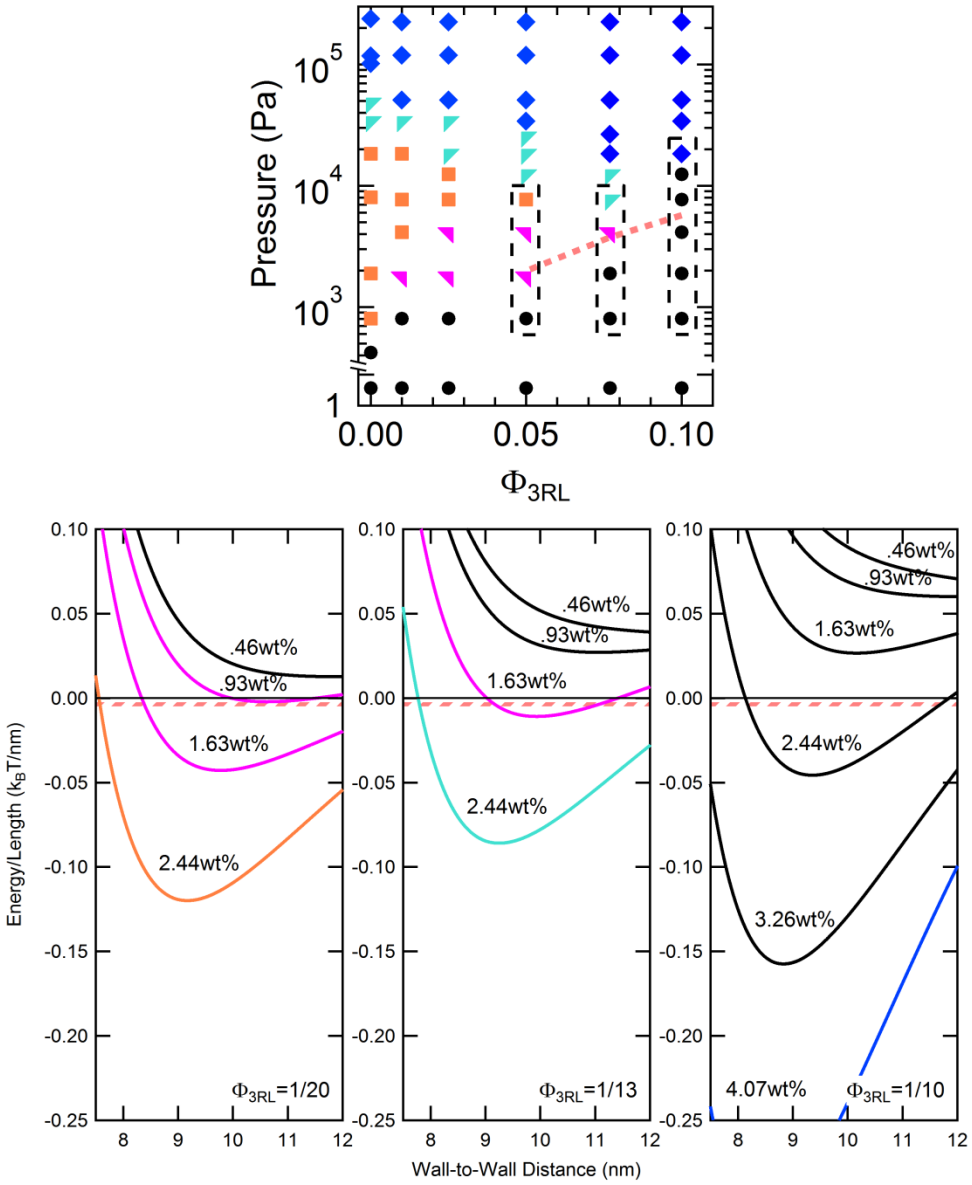

Figure S2.4| The charged brush model for 3RL Tau at higher coverages of Tau is in closer agreement with experimental behavior. At osmotic pressures taken from selected experimental data points (top), the normalized potential energy per unit length curves were plotted for Φ_{3RL}=1/20, 1/13, 1/10 (bottom), with the color of each model curve corresponding to phase observed experimentally. The phase diagram (top) has been marked (pink-dashed line) at the pressure where bundling is expected, if bundling is assumed to occur at a potential energy depth of 7.5 k_BT for 2 µm length MTs (see Fig. S1.6). The potential energy curves (bottom) also have a pink-striped zone, which corresponds to a potential energy depth of 5 to 10 k_BT.

SI Figure S1

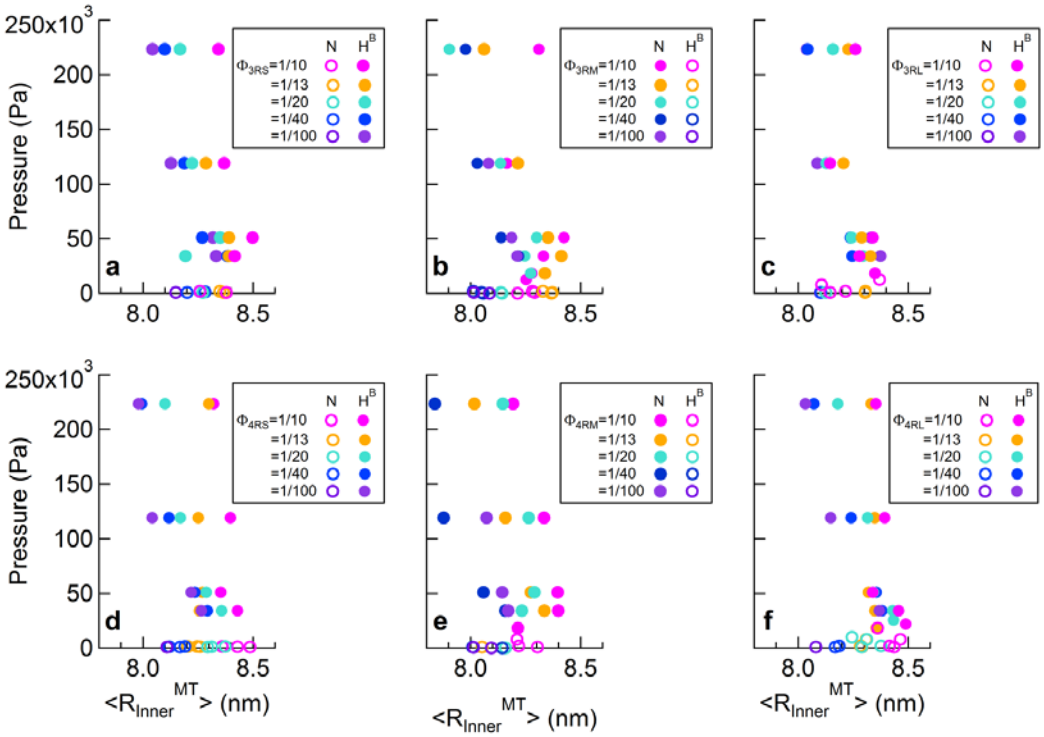

Increasing concentrations of Tau stabilize microtubule radii under increasing osmotic pressure. (**a-f**) The inner radii, a fit parameter, plotted as a function of increasing pressure for different reactions mixtures of (a) 3RS, (b) 3RM, (c) 3RL, (d) 4RS, (e) 4RM and (f) 4RL. For all isoforms, high molar concentrations of Tau led to stabilized inner radii (and thus, protofilament numbers) at pressures as high as 250,000 Pa. This behavior was not unique to any isoform, and was more a function of Tau molar concentration, indicating the effect that Tau MTBRs had on stabilizing the mechanical properties of MTs. The change in MT radius for lower coverages of Tau could possibly be due to either Tau falling off at higher osmotic pressures (leading to a concomitant decrease in MT radii (18)) or the stabilization of MTs with smaller radii at higher pressure.

SI Figure S2 – 1D X-ray scattering plots for Φ_{3RS}=1/10

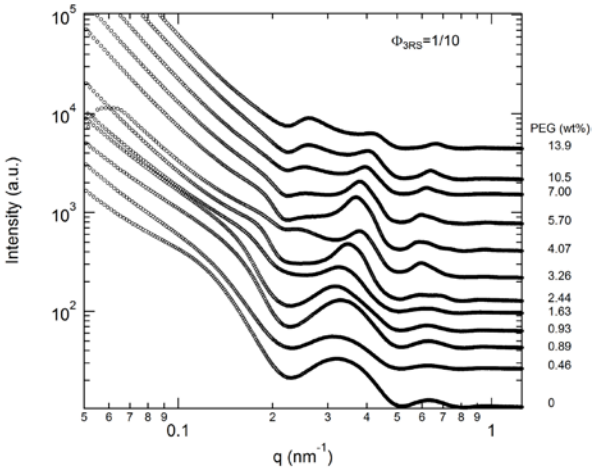

SI Figure S3 – 1D X-ray scattering plots for Φ_{3RS} =1/13

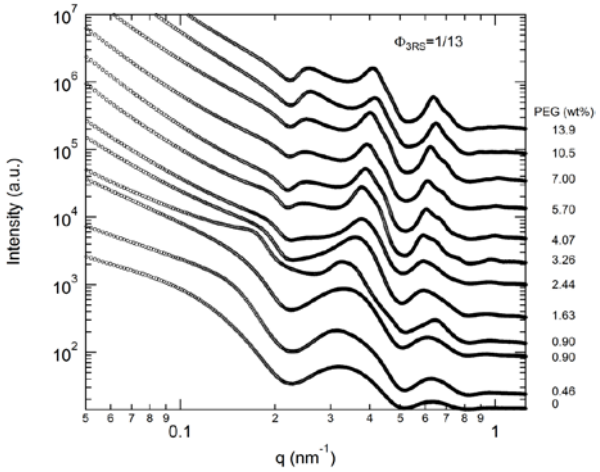

SI Figure S4 – 1D X-ray scattering plots for Φ_{3RS} =1/20

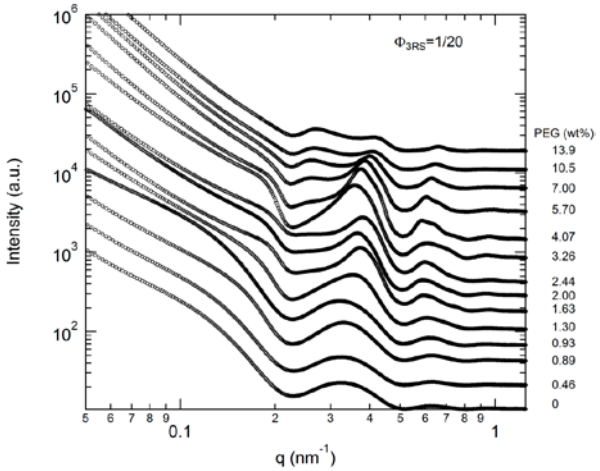

SI Figure S5 – 1D X-ray scattering plots for Φ_{3RS} =1/40

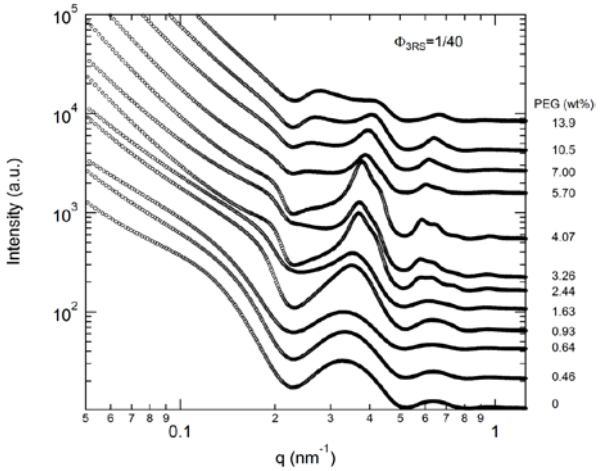

SI Figure S6 – 1D X-ray scattering plots for Φ_{3RS} =1/100

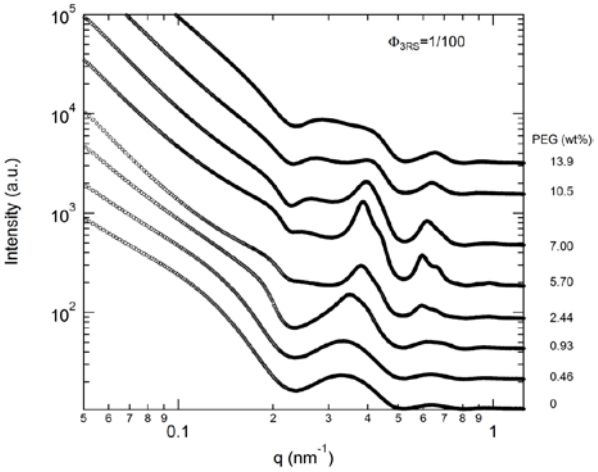

SI Figure S7 – 1D X-ray scattering plots for Φ_{3RM} =1/10

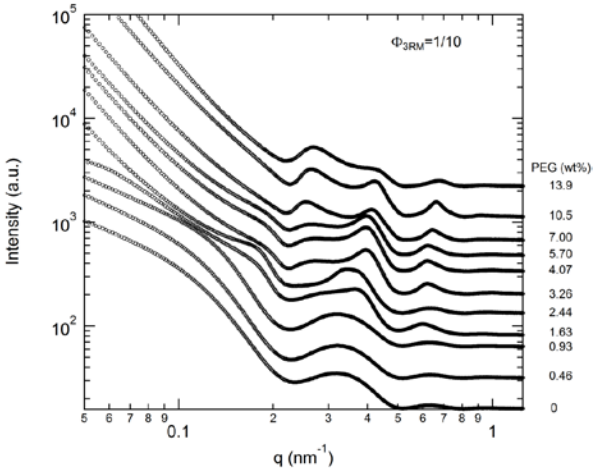

SI Figure S8 – 1D X-ray scattering plots for Φ_{3RM}=1/13

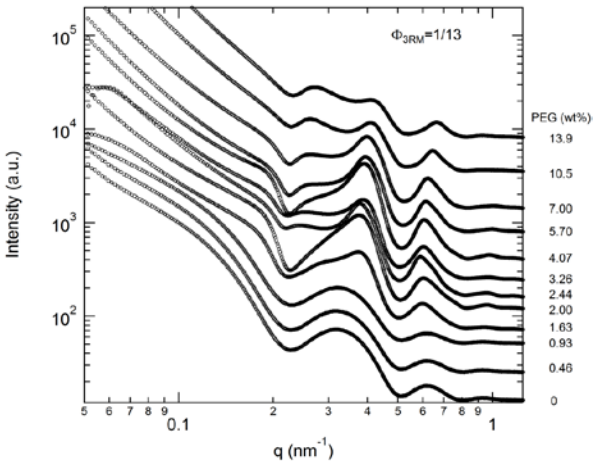

SI Figure S9 – 1D X-ray scattering plots for Φ_{3RM}=1/20

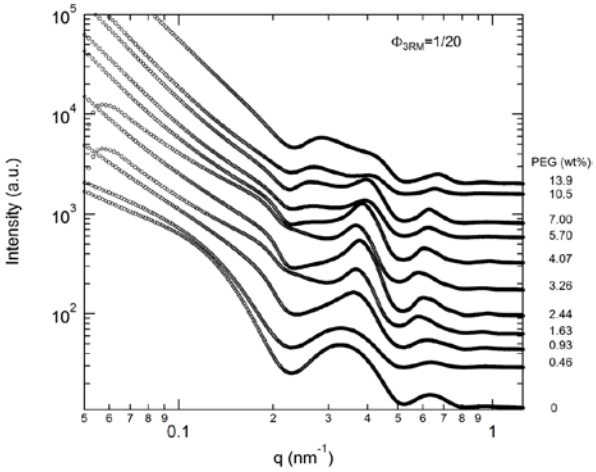

SI Figure S10 – 1D X-ray scattering plots for Φ_{3RM}=1/40

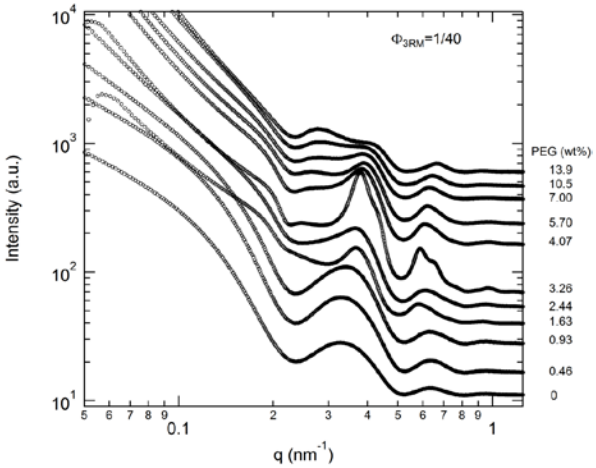

SI Figure S11 – 1D X-ray scattering plots for Φ_{3RM}=1/100

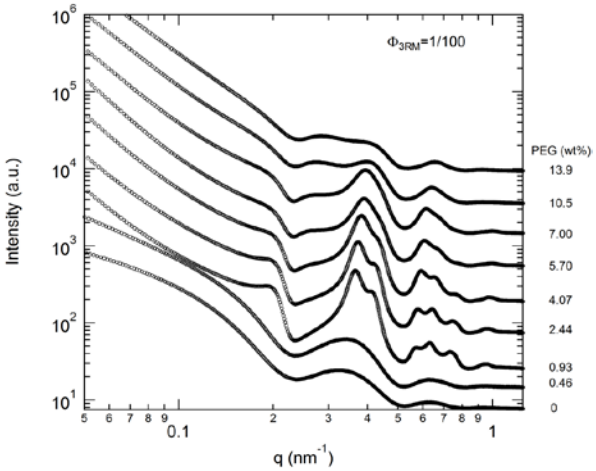

SI Figure S12 – 1D X-ray scattering plots for Φ_{3RL}=1/10

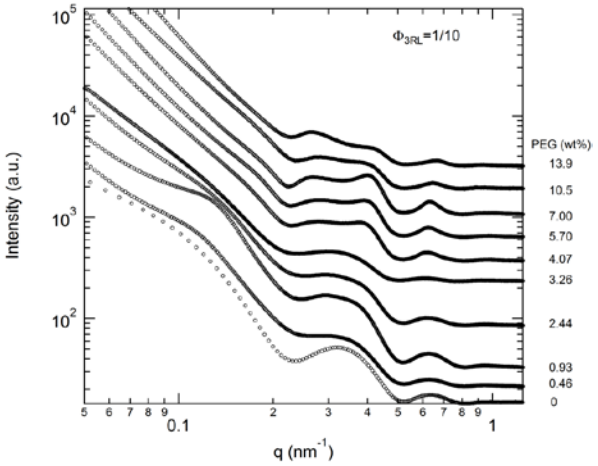

SI Figure S13 – 1D X-ray scattering plots for Φ_{3RL}=1/13

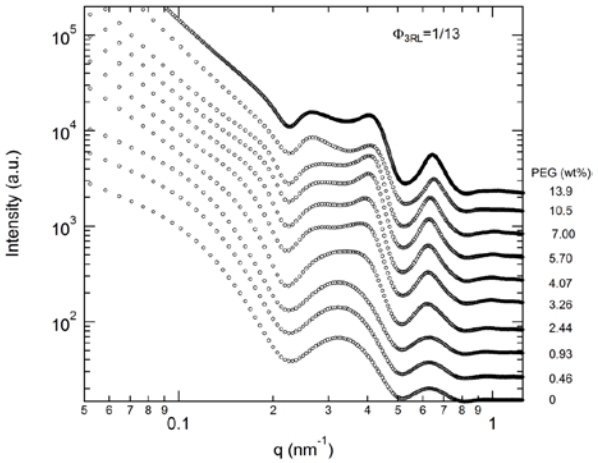

SI Figure S14 – 1D X-ray scattering plots for Φ_{3RL}=1/20

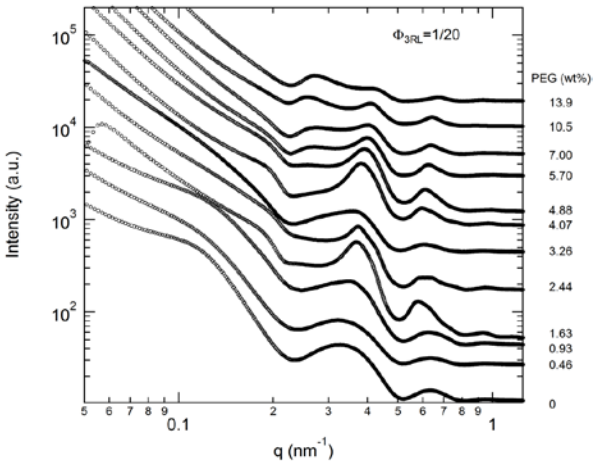

SI Figure S15 – 1D X-ray scattering plots for Φ_{3RL}=1/40

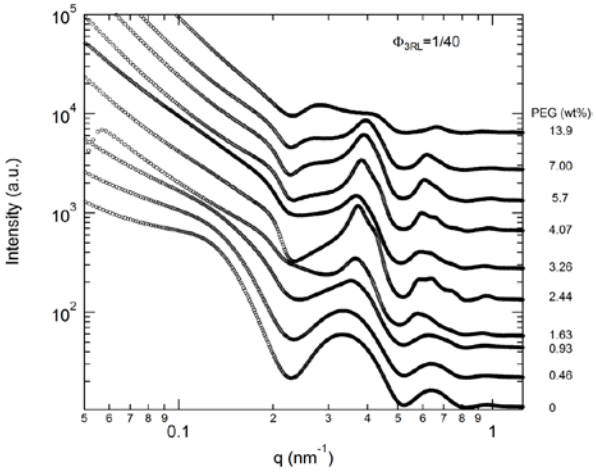

SI Figure S16 – 1D X-ray scattering plots for Φ_{3RL}=1/100

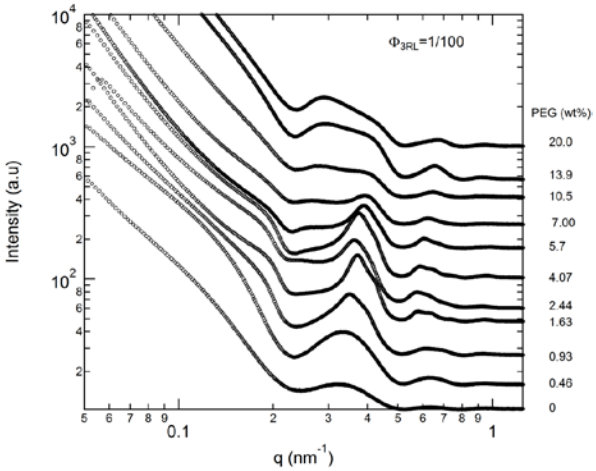

SI Figure S17 – 1D X-ray scattering plots for Φ_{4RS}=1/10

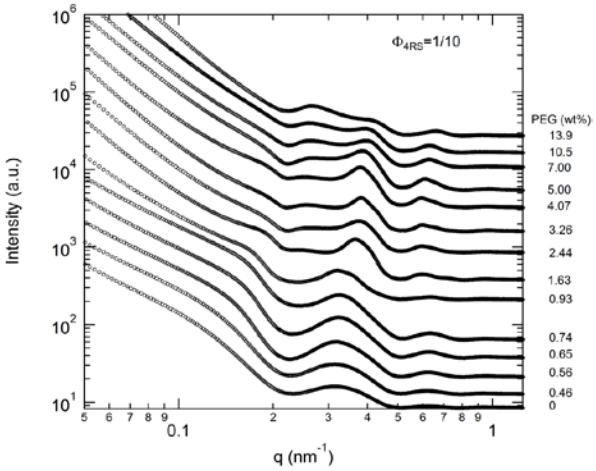

SI Figure S18 – 1D X-ray scattering plots for Φ_{4RS}=1/13

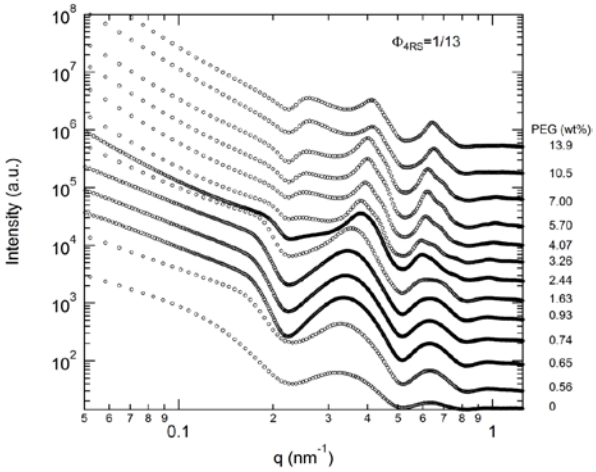

SI Figure S19 – 1D X-ray scattering plots for Φ_{4RS}=1/20

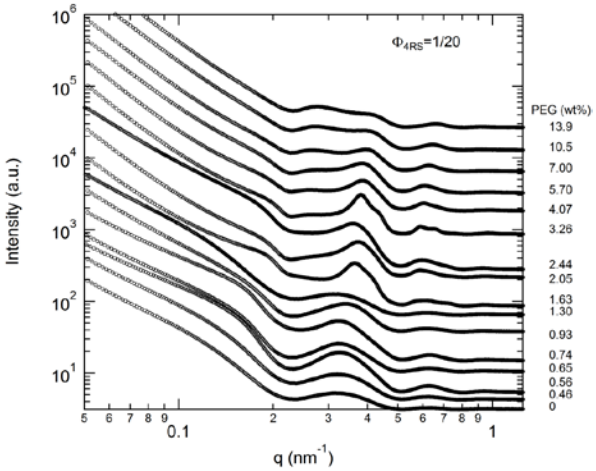

SI Figure S20 – 1D X-ray scattering plots for Φ_{4RS}=1/40

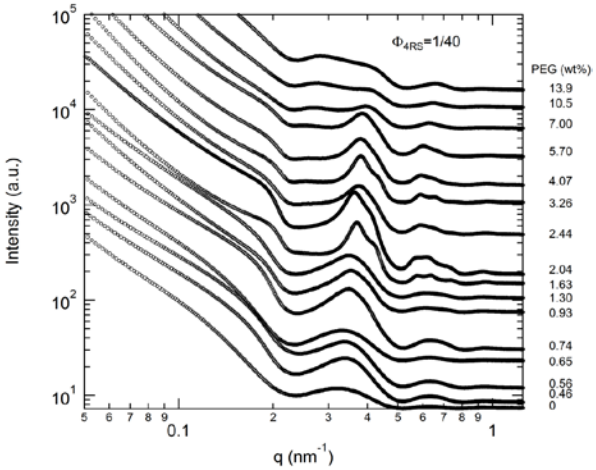

SI Figure S21 – 1D X-ray scattering plots for Φ_{4RS}=1/100

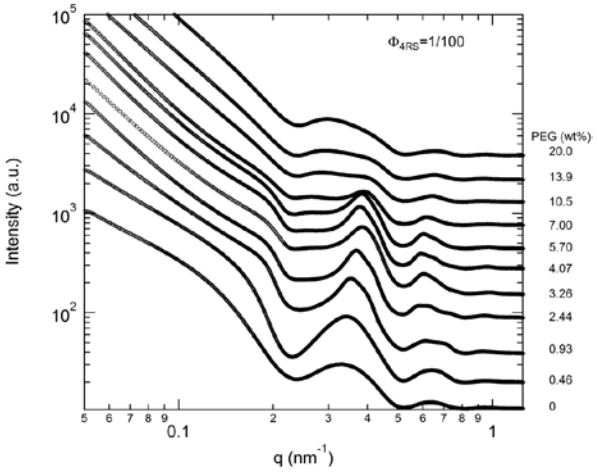

SI Figure S22 – 1D X-ray scattering plots for Φ_{4RM}=1/10

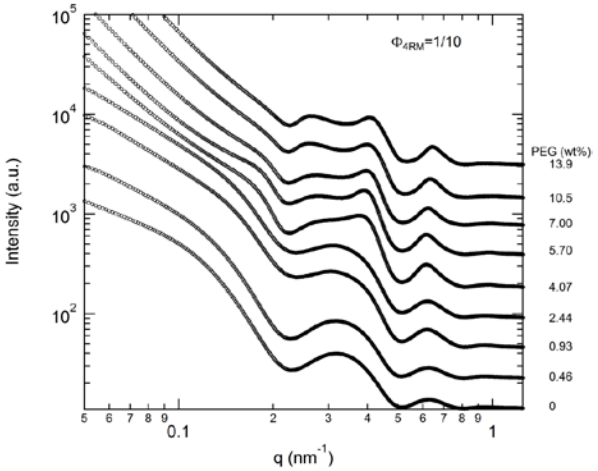

SI Figure S23 – 1D X-ray scattering plots for Φ_{4RM}=1/13

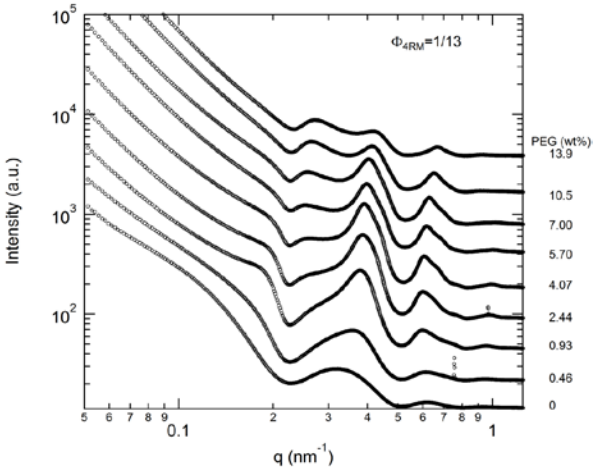

SI Figure S24 – 1D X-ray scattering plots for Φ_{4RM}=1/20

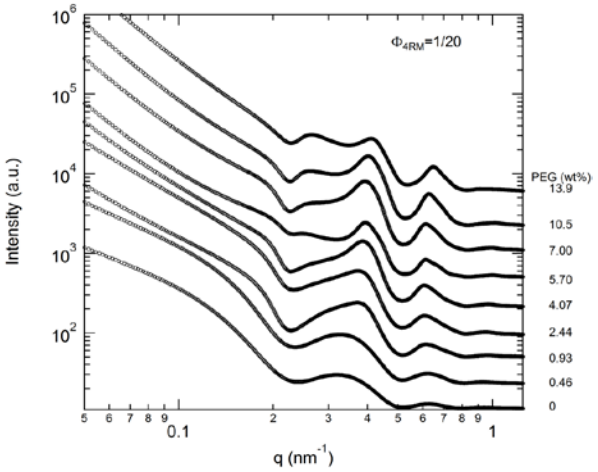

SI Figure S25 – 1D X-ray scattering plots for Φ_{4RM}=1/40

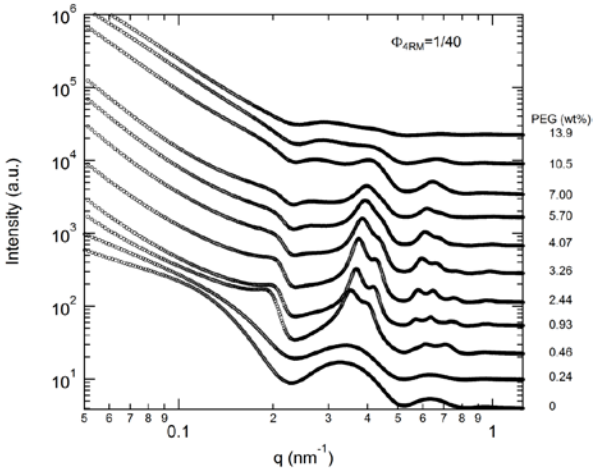

SI Figure S26 – 1D X-ray scattering plots for Φ_{4RM}=1/100

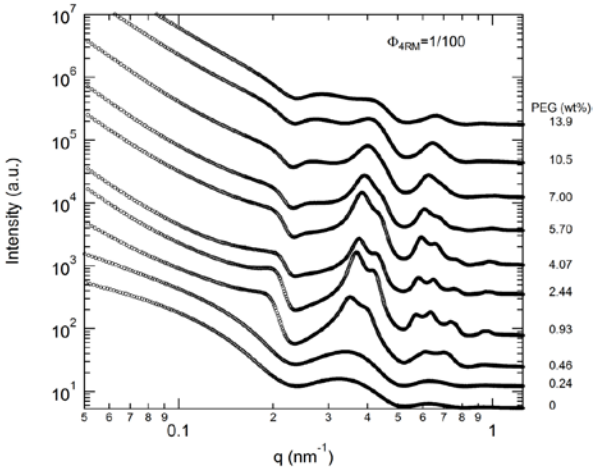

SI Figure S27 – 1D X-ray scattering plots for Φ_{4RL}=1/10

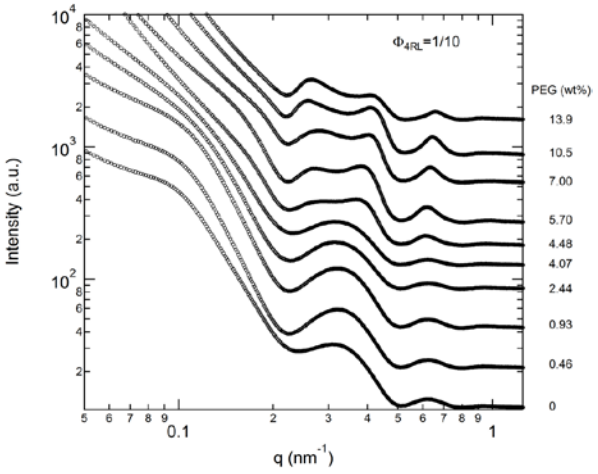

SI Figure S28 – 1D X-ray scattering plots for Φ_{4RL}=1/13

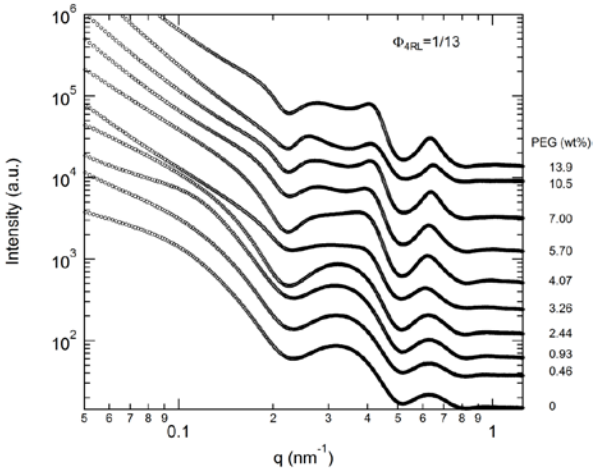

SI Figure S29 – 1D X-ray scattering plots for Φ_{4RL}=1/20

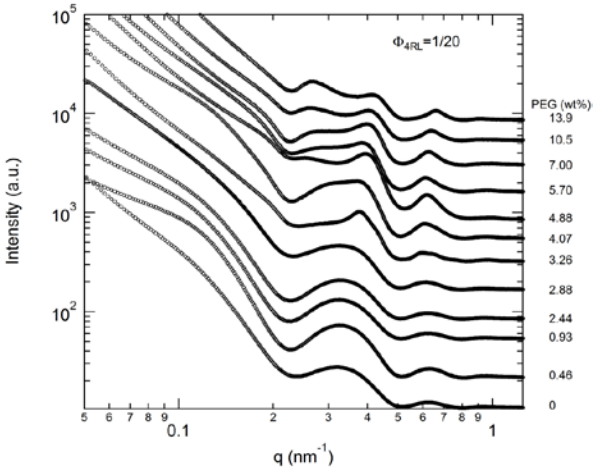

SI Figure S30 – 1D X-ray scattering plots for Φ_{4RL}=1/40

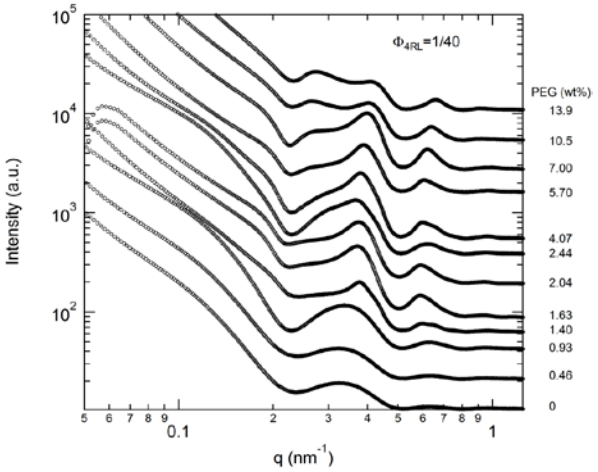

SI Figure S31 – 1D X-ray scattering plots for Φ_{4RL}=1/100

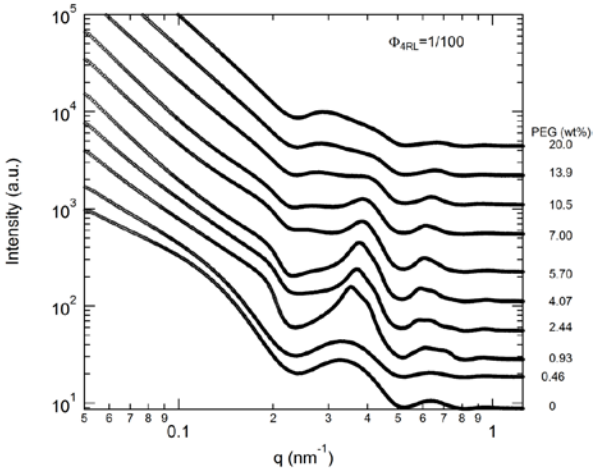

SI Figure S32 – 1D X-ray scattering plot for no Tau

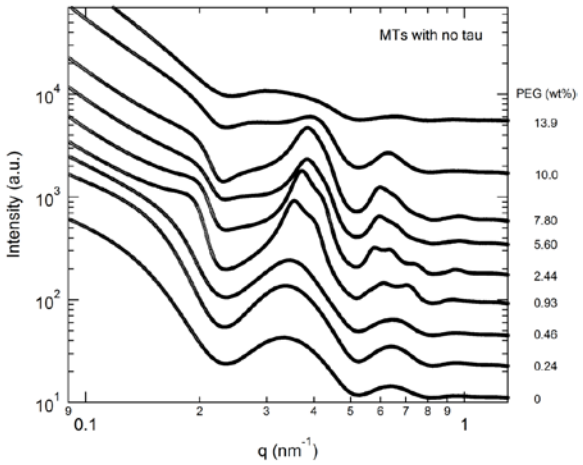

SI Appendix References

1. Israelachvili JN (1992) *Intermolecular & Surface Forces* (Academic Press Limited). 2nd Ed.
2. Asakura S, Oosawa F (1958) Interaction between particles suspended in solutions of macromolecules. *J Polym Sci* 33(126):183–192.
3. Tuinier R, Fleer GJ (2004) Concentration and solvency effects on the pair interaction between colloidal particles in a solution of nonadsorbing polymer. *Macromolecules* 37(23):8764–8772.
4. Devanand K, Selser JC (1991) Asymptotic Behavior and Long-Range Interactions in Aqueous Solutions of Poly (ethylene oxide). *Macromolecules* 24(22):5943–5947.
5. Jones CW, Wang JC, Ferrone FA, Briehl RW, Turner MS (2003) Interactions between sickle hemoglobin fibers. *Faraday Discuss* 123:221–236; discussion 303–322, 419–421.
6. Rand RP Osmotic Stress. Available at: //www.brocku.ca/ researchers/peter_rand/osmotic/osfile.html#data.
7. Derjaguin B, Landau L (1993) Theory of the stability of strongly charged lyophobic sols and of the adhesion of strongly charged particles in solutions of electrolytes. *Prog Surf Sci* 43(1-4):30–59.
8. Ohshima H, Hyono A (2009) Electrostatic interaction between two cylindrical soft particles. *J Colloid Interface Sci* 333(1):202–208.
9. Van den Heuvel MGL, de Graaff MP, Lemay SG, Dekker C (2007) Electrophoresis of individual microtubules in microchannels. *Proc Natl Acad Sci U S A* 104(19):7770–7775.
10. Sackett DL (1995) Structure and function in the tubulin dimer and the role of the acidic carboxyl terminus. *Subcell Biochem* 24:255–302.
11. Carlier MF, Pantaloni D (1983) Taxol effect on tubulin polymerization and associated guanosine 5’-triphosphate hydrolysis. *Biochemistry* 22(20):4814–4822.
12. Ludueña RF (2013) A Hypothesis on the Origin and Evolution of Tubulin. *Int Rev Cell Mol Biol* 302:41–185.
13. Tuszyński JA, et al. (2005) Molecular dynamics simulations of tubulin structure and calculations of electrostatic properties of microtubules. *Math Comput Model* 41(10):1055–1070.
14. Christos GA, Carnie SL, Creamer TP (1992) Monte Carlo simulations of partially ionized polyelectrolytes: conformational properties. *Macromolecules* 25(3):1121–1124.
15. Chen J, Kanai Y, Cowan NJ, Hirokawa N (1992) Projection domains of MAP2 and tau determine spacings between microtubules in dendrites and axons. *Nature* 360(6405):674–677.
16. Leermakers FAM, Jho Y-S, Zhulina EB (2010) Modeling of the 3RS tau protein with self-consistent field method and Monte Carlo simulation. *Soft Matter* 6(21):5533.
17. Jho YS, Zhulina EB, Kim MW, Pincus PA (2010) Monte Carlo simulations of tau proteins: Effect of phosphorylation. *Biophys J* 99(8):2387–2397.
18. Choi MC, et al. (2009) Human microtubule-associated-protein tau regulates the number of protofilaments in microtubules: A synchrotron X-ray scattering study. *Biophys J* 97(2):519–527.
19. Witten TA, Pincus P (2007) Structure and Viscosity of Interpenetrating Polyelectrolyte Chains. *Europhys Lett* 3(3):315–320.
20. Pincus P (1991) Colloid stabilization with grafted polyelectrolytes. *Macromolecules* 24(10):2912–2919.